Automated Design and Miniaturization of RF Resonators Based on the Cesàro Fractal for Chipless RFID Tags

Gabriel São Martinho Da Silva, Rodrigo Luiz Ximenes, Lisandro Manuel De la Torre Rodríguez, and Leonardo Lorenzo Bravo Roger

***Abstract*—This paper presents an automated methodology for the design of compact modified Cesàro fractal resonators. Python scripts integrated with HFSS are used to generate these structures, offering a compact alternative to conventional square-loop resonators for chipless RFID tags through iterative size reduction. Unlike the Koch curve, which is constrained to a fixed 60° indentation angle, the Cesàro fractal allows this angle to be freely adjusted as a design parameter, enabling greater geometric flexibility and control over the resonant frequency. The proposed methodology encompasses theoretical fractal analysis, script-driven geometry generation, full-wave electromagnetic simulation, fabrication, and experimental validation. Results demonstrate precise control over the resonant frequency, and experimental validation confirms the Cesàro fractal as an efficient, compact alternative to square-loop resonators for high-performance chipless RFID systems.**

Link to graphical and video abstracts, and to code:
https://latamt.ieeer9.org/index.php/transactions/article/view/10722

***Index Terms*—Chipless RFID, fractal resonator, Cesàro fractal, miniaturization, electromagnetic simulation, HFSS, Python**

I. Introduction

RADIO FREQUENCY IDENTIFICATION (RFID) technology has become ubiquitous in modern automatic identification systems, enabling wireless data exchange between tags and readers via backscattered radio waves [1]. Among the various RFID implementations, chipless RFID tags have garnered significant attention due to their potential for low cost fabrication, as they eliminate the need for silicon integrated circuits [2]. This makes them particularly attractive for item-level tracking in logistics, retail, and healthcare applications within the Internet of Things (IoT) paradigm [3].

In chipless RFID systems, information is encoded through the interaction between the reader's interrogating signal and the physical structure of the tag itself. Two primary encoding approaches are commonly employed: time-domain encoding, which relies on delay lines, and frequency-domain encoding using resonant structures. This paper focuses on the latter, where multiple resonators are coupled to a transmission line to create distinct frequency signatures that represent binary data.

Fig. 1 illustrates a canonical square-loop resonator coupled to a microstrip transmission line, a fundamental building block in frequency-domain chipless tags.

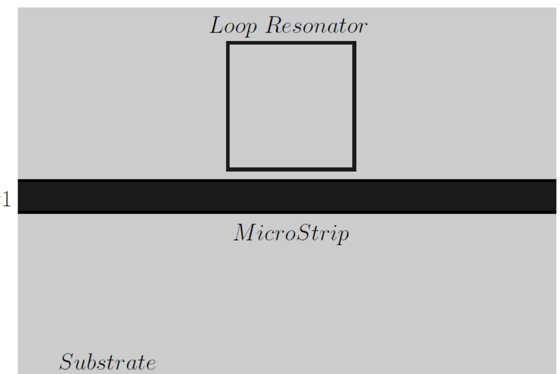

Fig. 1. Square-Loop Resonator Configuration.

Due to the inductive coupling between the microstrip feed line and the square-loop resonator, when the resonator resonates at a specific frequency, it extracts energy from the wave propagating along the microstrip line. This increases the current density level on the resonator while decreasing it on the line. As a result, a pronounced attenuation (notch) appears at that frequency in the S_{21} curve. In this case, a low current level reaches port 2, a situation defined as a logic "0" state, shown in Fig. 2 (a).

Conversely, when resonance does not occur, there is minimal coupling between the line and the resonator. The current density level remains high on the line and low on the resonator. Consequently, the S_{21} curve exhibits low attenuation, and a high current level reaches port 2, corresponding to a logic "1" state, as shown in Fig. 2 (b). This binary encoding mechanism forms the foundation of frequency-domain chipless RFID systems [4].

The encoding of multibit codewords requires the coupling of multiple resonators to the microstrip line, which inevitably increases the overall footprint of the tag. Since the resonant frequency of a loop resonator is fundamentally determined by its perimeter, a common miniaturization strategy involves the use of fractal geometries [5]. These structures can maintain a constant electrical length (perimeter) while occupying a significantly reduced physical area, making them attractive for

The associate editor coordinating the review of this manuscript and approving it for publication was Roberto S. Murphy (*Corresponding author: Gabriel São Martinho da Silva*).

This work was supported in part by CAPES – Finance Code 001.

Gabriel São Martinho da Silva, R. L. Ximenes, L. M. De la T. Rodríguez, and L. L. Bravo-Roger are with the Faculty of Technology, University of Campinas, Limeira, São Paulo, Brazil (e-mails: g216465@dac.unicamp.br, ximenes@unicamp.br, lisandro@decom.fee.unicamp.br, and leobravo@unicamp.br).

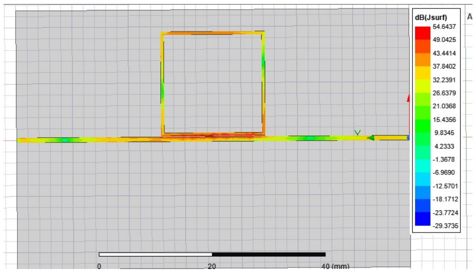

(a)

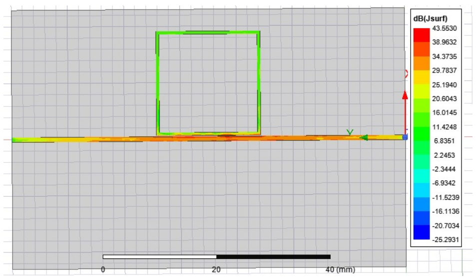

(b)

Fig. 2. (a) Square loop resonator, bit 0. (b) Square loop resonator, bit 1.

compact RF devices. Chipless RFID systems employ fractal structures due to their unique geometric properties. The self-similarity property enables the creation of complex configurations through pattern repetition, allowing the design of compact resonators capable of operating at multiple frequencies without requiring large physical footprints. In chipless RFID systems, this facilitates the development of tags with increased data storage capacity or enhanced operational efficiency, even within severely constrained spaces. On printed circuit boards, fractals enable the realization of surfaces that can filter, reflect, or transmit radio signals across multiple frequency bands. Furthermore, fractal structures can enhance key performance characteristics such as miniaturization and bandwidth.

II. Related Work

Recent advances in chipless RFID have explored various resonator geometries to achieve compactness and spectral efficiency. Square-loop resonators remain the most prevalent due to their simplicity and well-understood behavior. However, the growing demand for miniaturized and high-capacity tags has motivated the investigation of fractal geometries, which exploit self-similarity to increase electrical length within a reduced physical area.

Among the most studied approaches, Koch fractal curves have been applied to complementary split ring resonators (CSRRs) in composite right/left-handed transmission lines [6], where first and second order iterations yielded resonant frequency reductions of 22% and 34%, respectively, while preserving the outer dimensions of the resonator (l = 11 mm). Minkowski fractal resonators have also been widely explored for sensor and filter applications: Nantapanich et al. [7] proposed a second-order NP-model Minkowski resonator in microstrip technology that resonates at 2.936 GHz within a 12.50×12.50 mm footprint. In a related direction, Govindankutty et al. [8] demonstrated that square-shaped fractal patterns applied to open complementary split ring resonators (OCSRRs) on a single conducting layer can reduce the resonant frequency from 920 MHz to 485 MHz across two iterations a 47.3% reduction, while keeping the physical dimensions unchanged. Beyond these, Hilbert [9] [10] and Moore [11] curve geometries have also demonstrated significant electrical length increase within constrained areas, further expanding the design space for compact resonators. In the context of UHF RFID applications, Jalal et al. [12] proposed a Minkowski fractal tag achieving a read range of 2.17 m with compact dimensions, highlighting the practical viability of fractal geometries beyond laboratory conditions.

Despite these advances, the geometries discussed above still exhibit limited design flexibility, as their parameters are typically fixed or allow only narrow tuning ranges. In this context, the Cesàro fractal emerges as a promising yet underexplored alternative. Unlike the Koch curve, which is constrained to a fixed 60° angle, the Cesàro fractal introduces a tunable deformation angle, enabling finer control over the resonant frequency and miniaturization.

In addition, the practical use of fractal resonators is limited by two main challenges: the largely manual design process, which requires multiple simulation iterations, and the restricted parametric control of conventional geometries, making fine tuning difficult without altering the overall footprint an issue that becomes critical in compact multibit tags.

To overcome these limitations, this work proposes an automated Python-based framework for generating Cesàro fractal resonators. The approach enables systematic control of the resonant frequency through perimeter variation (coarse tuning) and angle adjustment (fine tuning). Experimental results confirm that the proposed resonators achieve significant size reduction while maintaining performance comparable to conventional square-loop designs.

III. Methodology

The methodology of this work is divided into three main parts. (A) ”Cesàro Fractal Geometry and Construction”, which presents the mathematical formulation used to generate the fractal structures studied in this work. (B) ”Parametric Design Automation Using Python and HFSS”, where the Python script developed for the automated generation of resonator geometries is described. Finally, (C) ”Prototype Fabrication of the Resonators”, which details the procedures used for the physical fabrication of the proposed resonator structures.

A. Cesàro Fractal Geometry and Construction

To analyze the geometric aspects involved in the construction of these structures, it is necessary to first define the variables associated with the Cesàro curve. Fig. 3 illustrates the main geometric parameters of the Von Koch and Cesàro curves. The total length of the fractal curve after n iterations (L_n) is indicated in blue, the length of the initial straight-line segment (L) in red, and the length of each segment of the fractal curve (l) in yellow.

The Cesàro curve can be regarded as a generalization of the Von Koch curve. In the classical Koch construction, the indentation angle is fixed at 60°, whereas in the Cesàro curve this angle can assume different values. This additional degree of freedom allows greater geometric flexibility in the construction of fractal structures.

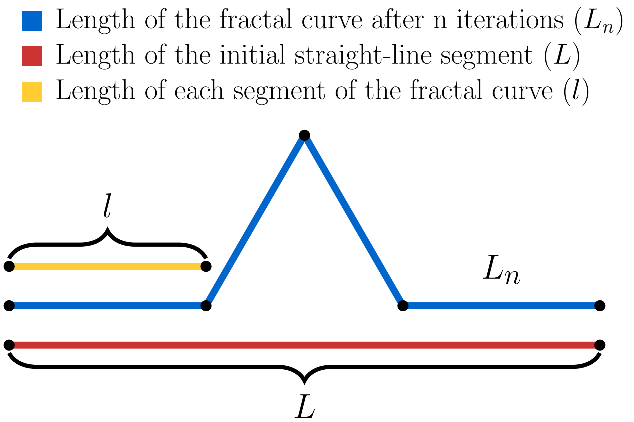

Fig. 3. Variables of the Cesàro fractal curve: length of the fractal curve after n iterations (L_n, blue), length of the initial straight-line segment (L, red), and length of each segment of the fractal curve (l, yellow).

For clarity, the construction of the Von Koch curve is first reviewed, since it corresponds to a particular case of the Cesàro curve.

Fig. 4 illustrates the iterative construction procedure. In step (1), a straight line segment is defined as the zeroth-order element (n = 0). In step (2), this segment is divided into three equal parts, and the central segment is selected for modification. In step (3), the selected segment is replaced by two segments forming an equilateral triangle, ensuring that all resulting segments have equal length.

In step (4), the same procedure is recursively applied to each segment obtained in the previous stage, dividing every segment into three equal parts and selecting their middle portions for modification. Finally, in step (5), each of these middle segments is replaced by two segments forming new equilateral triangles. By repeating this recursive process, the fractal order increases progressively, generating the well-known Von Koch curve.

Based on Fig. 4, it can be observed that the number of segments increases according to 4^n, where n denotes the fractal order. Additionally, at each iteration, every segment is divided into three equal parts. Consequently, the length of each segment, denoted by l, is given by $l = L/3^n$ where L represents the length of the initial straight-line segment.

From these two results, a general expression for the total length of the Von Koch curve after n iterations, L_n, can be obtained, as given in (1).

$$L_n = \left(\frac{4}{3}\right)^n \times L \tag{1}$$

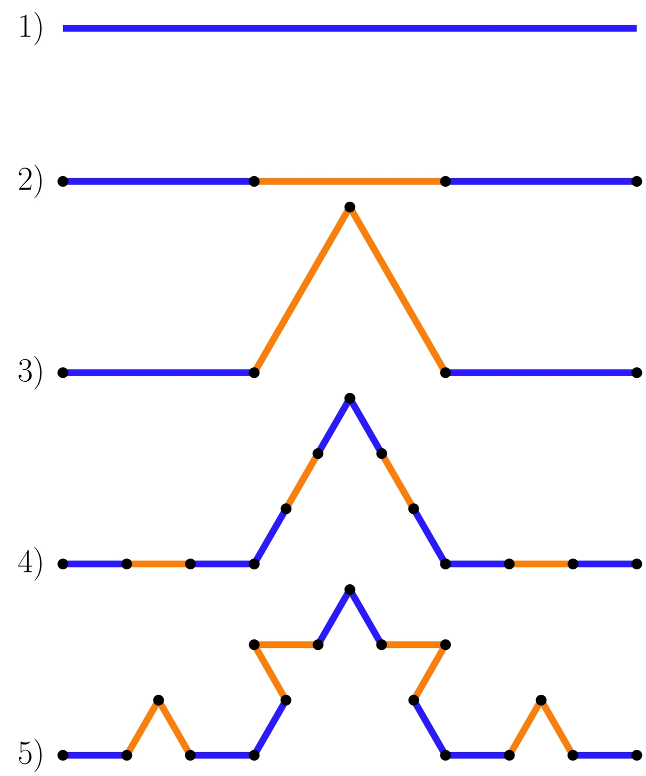

Fig. 4. Von Koch curve construction process.

The difference between the Von Koch curve and the Cesàro curve lies in the geometric construction of the triangle, specifically in the value of its base. In the Von Koch curve, the triangle is equilateral, therefore, all sides, including the base, have equal length. In contrast, the Cesàro curve employs an isosceles triangle. Although all constructed segments have equal length l, the base of the isosceles triangle differs from the other sides. Consequently, this geometric modification leads to a reformulation of (1), resulting in (2), and Table I shows how the number of segments increases with the iteration order and how the length of each segment changes as a function of the angle θ and the order n of Cesàro's fractal curve

$$L_n = \left(\frac{4}{(2 \times (\cos(\theta) + 1))}\right)^n \times L \tag{2}$$

TABLE I
NUMBER OF SEGMENTS AND LENGTH VALUES OF THE CESÀRO CURVE

Order	Number of segments	Segment lengths (l)
0	1	$l = L$
1	4^1	$l = L/(2 \times (\cos(\theta) + 1))^1$
2	4^2	$l = L/(2 \times (\cos(\theta) + 1))^2$
3	4^3	$l = L/(2 \times (\cos(\theta) + 1))^3$
4	4^4	$l = L/(2 \times (\cos(\theta) + 1))^4$
5	4^5	$l = L/(2 \times (\cos(\theta) + 1))^5$
...	...	...
n	4^n	$l = L/(2 \times (\cos(\theta) + 1))^n$

Fig. 5 illustrates the first-order fractal design investigated in this study, in which the base geometry was modified to enhance the coupling efficiency between the resonator and the microstrip line. Variations in the indentation angle allow the

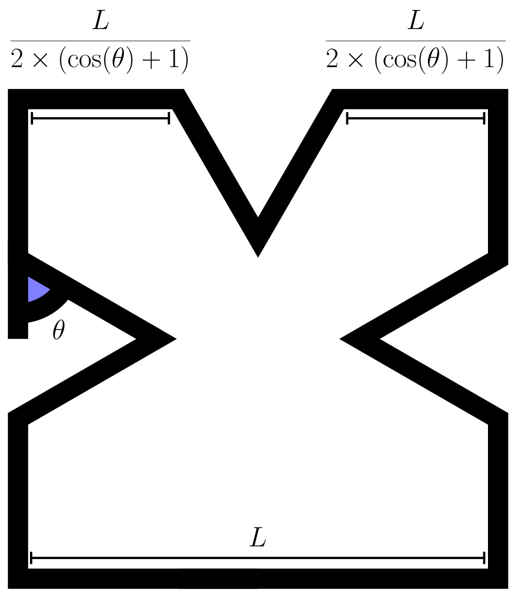

Fig. 5. The fractal proposal made in this study.

area of the fractal structure to decrease while the perimeter remains constant. This property can be exploited to achieve structural miniaturization without altering the total electrical length of the resonator. Therefore, the main objective of this work is to investigate how angular variation can be used for miniaturization while also analyzing the influence of the perimeter and angle parameters on the resonance frequency of the fractal geometry. Fig. 6 illustrates the progressive evolution of the fractal structure for angular increments of 10 degrees. Although all configurations maintain the same total perimeter, a noticeable reduction in the effective area occupied by the resonator is observed as the angle increases. This geometrical compression results in a more compact footprint, which is particularly advantageous in chipless RFID applications, where size reduction is often a key design requirement. Furthermore, this controlled angular variation introduces an additional degree of freedom for adjusting the electromagnetic response of the structure without modifying its total perimeter.

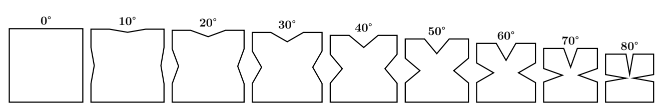

Fig. 6. Evolution of the fractal structure by modifying the angle and maintaining the perimeter of the resonator.

B. Parametric Design Automation Using Python and HFSS

A Python script was developed to automate the generation of fractal structures in HFSS. Fig. 7 shows these structures constructed in HFSS: in (a) a first-order resonator, while in b) there is a second-order resonator. In both cases, the resonator and microstrip line are depicted in black (copper) over a white FR4 substrate, with a ground plane located beneath the structure. The script parametrically generates the geometry from user-defined input variables, enabling systematic control of parameters such as fractal order and angle. This approach eliminates the need for manual, step by step modeling of each configuration, the automation facilitates rapid iteration and optimization studies, making the exploration of multiple geometric variations more efficient.

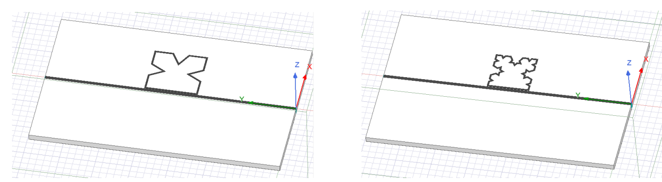

(a) (b)

Fig. 7. a) First-order resonator. b) Second-order resonator.

The Python code implementing the algorithm used to generate the fractal geometries presented in this work is available at the following repository. The shared implementation corresponds to the portion of the code responsible for the parametric generation of the fractal structures used in this study: https://github.com/gabrielsaomartinhosilva-hue/CesaroFractal/tree/main.

C. Prototype Fabrication of the Resonators

After the simulation phase, three first-order prototypes (0°, 45°, and 60°) and one second-order prototype (60°) were fabricated using chemical etching. A DXF file from HFSS was edited in AutoCAD and printed on transfer paper. The FR4 substrates were cleaned, cut, thermally pressed at 200 °C for 2 min, etched in ferric chloride, cleaned, and fitted with SMA connectors. Frequency sweeps were then measured with a VNA (Fig. 8). The FR4 substrates were experimentally characterized [13], resulting in a relative permittivity of $\varepsilon_r = 3.9$ and a loss tangent of $\tan\delta = 0.05$.

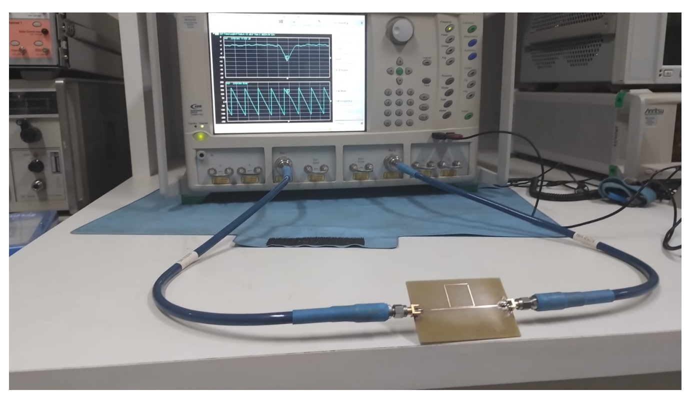

Fig. 8. Vector network analyzer measuring the resonance frequencies of the constructed prototypes.

IV. Results and Discussion

The results of this work are presented in two main parts:

(A) "Influence of Design Parameters on the Resonant Frequency" which focuses on a parametric study of the proposed structure. In this section, the main geometric parameters are varied to observe their influence on the resonance frequency obtained from electromagnetic simulations. This analysis allows for a qualitative and comparative understanding of how the design behaves under different configurations.

(B) "Comparison Between Simulated and Fabricated Prototypes" where the fabricated resonators are experimentally evaluated and their behavior is compared with the corresponding simulated models. This section aims to provide a general validation of the proposed approach, relating practical measurements to the expected simulation results.

A. *Influence of Design Parameters on the Resonant Frequency*

This section analyzes how variations in the perimeter and angular parameters of the first-order Cesàro fractal affect the resonant frequency of the resonator. To illustrate these effects, two graphs are presented.

Fig. 9 shows the relationship between the perimeter values, ranging from 60 to 80 mm in 1 mm increments, and the resonant frequency (GHz), sampled at 0.1 GHz intervals. The plotted curves correspond to the square loop resonator (0°) in green, and the fractal geometries with angles of 45° and 60° in blue and black, respectively.

The results indicate an inverse relationship between the perimeter and the resonant frequency. As the perimeter increases, the effective electrical length of the resonator also increases, resulting in a decrease in the resonant frequency. This behavior confirms that frequency tuning can be achieved by adjusting the geometric parameters of the structure. Fig. 10 shows how angular variation in the first-order fractal affects the resonance frequency. It presents three curves: the yellow curve corresponds to fractals with a perimeter of 60 mm, the orange curve represents those with a total perimeter of 70 mm, and the blue curve corresponds to fractals with a perimeter of 80 mm. The figure displays angle variations from 0° to 70° in 1° increments, while the vertical axis indicates the resonance frequency in GHz.

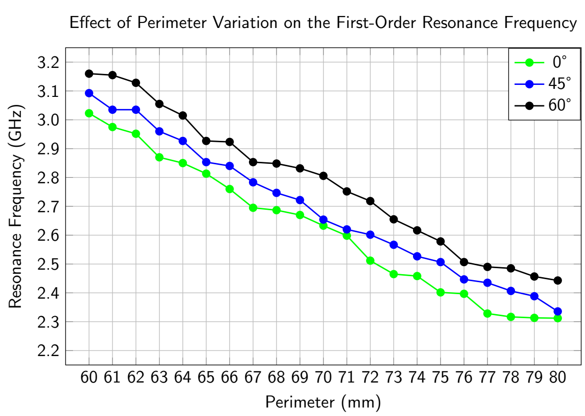

Fig. 9. Influence of the Perimeter on the Resonant Frequency.

The results indicate that the resonance frequency remains nearly constant, showing only a slight increase as the angle increases. This suggests that the structure's resonance frequency can leverage variations in the angle as a parameter for fine-tuning the resonance frequency.

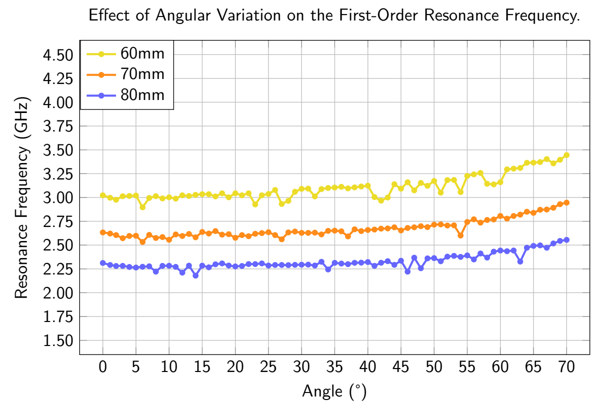

Fig. 10. Influence of the Angle on the Resonant Frequency.

B. *Comparison Between Simulated and Fabricated Prototypes*

This section presents the measured results of the analyzed resonators through tables and plots comparing simulated S_{21} [dB] responses obtained in HFSS (green curves) with measurements from a vector network analyzer (VNA) (red curves), Fig. 11 and Fig. 12 show the main simulation parameters of the first-order and second-order prototypes, respectively. Some variables are not depicted because the figure is two-dimensional while the prototype is three-dimensional. These include W_f (width of the fractal base and segments), H (PCB thickness), and t (copper thickness on both the top conductive layer and the ground plane).

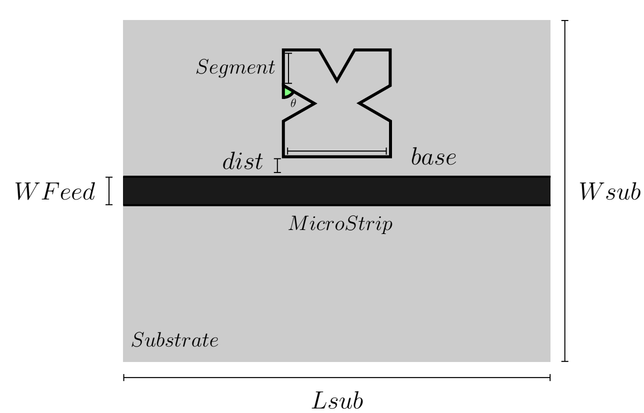

Fig. 11. Main variables of the first-order resonator.

The prototypes were then built as shown in the following figures, for all resonators, a total perimeter of 70 mm was used. Fig. 13 presents the square loop resonator together with the first-order fractals at angles of 45 and 60 degrees. Meanwhile, Fig. 14 illustrates the full potential of the code by generating

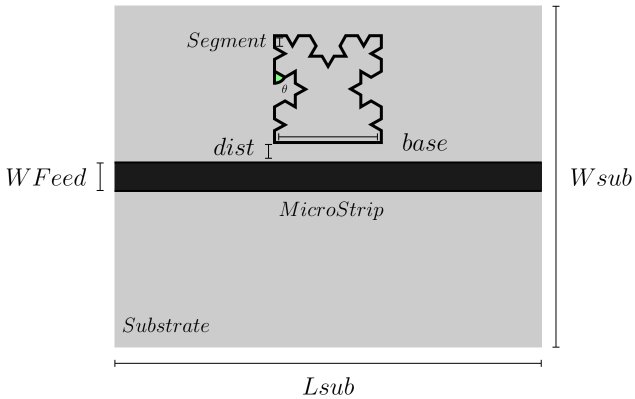

Fig. 12. Main dimensions of the second-order fractal resonator

a second-order resonator with a 60-degree angle, resulting in a significantly more complex structure.

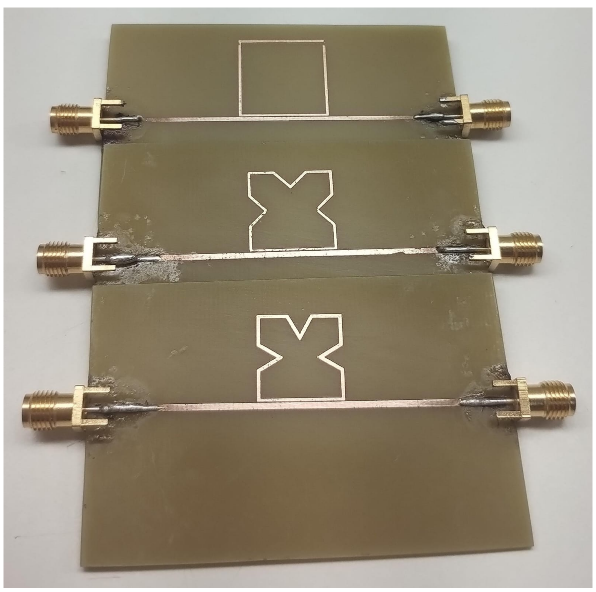

Fig. 13. Square loop resonator with 45 and 60 degree resonators of order 1.

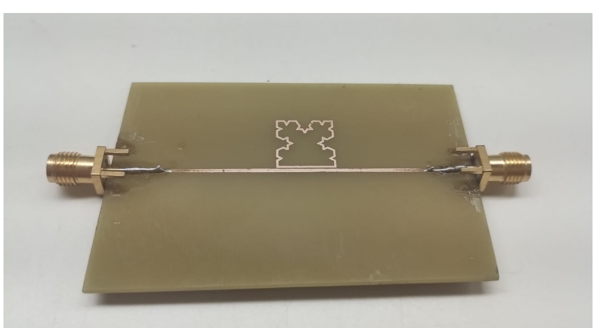

Fig. 14. 60-degree second-order resonator.

With the resonators constructed, four graphs were created comparing the measured and simulated values for each of the resonators presented, these comparisons are shown below.

Fig. 15 compares the simulated and measured results for the square loop resonator. The green curve, representing the HFSS simulation, shows a resonance frequency of 2.6330 GHz with an S_{21} value of -11.1043 dB. In contrast, the red curve, corresponding to the VNA measurements, indicates a resonance frequency of 2.6400 GHz with an S_{21} value of -12.4574 dB.

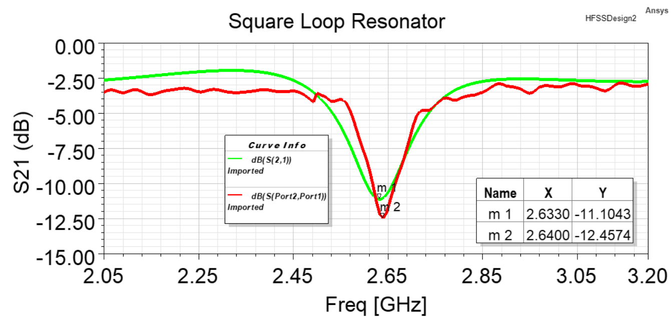

Fig. 15. Comparison of measured and simulated values for the square loop resonator.

Fig. 16 shows the simulated and corresponding measured responses for the first-order and 45° resonator. The green curve, representing the HFSS simulation, indicates a resonant frequency of 2.6540 GHz with an S_{21} value of -8.4840 dB. In contrast, the red curve, corresponding to the VNA measurements, shows a resonant frequency of 2.6595 GHz with an S_{21} value of -9.4731 dB. Abrupt discontinuities in the current path are observed, the current distribution in the resonator is not uniform, its effective impedance changes, resulting in a mismatch between the line and the resonator, leading to a less negative S_{21} value compared to the square loop.

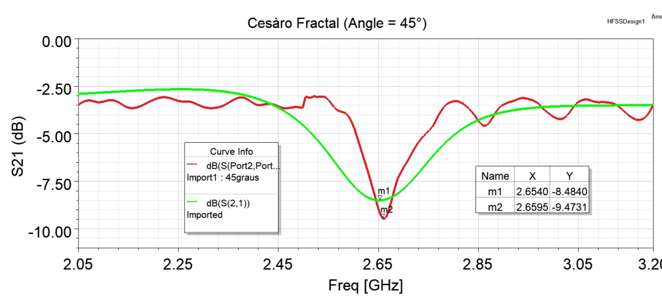

Fig. 16. Comparison of measured and simulated values for the 45-degree resonator.

Fig. 17 shows the comparison between the simulated and measured responses for the first-order, 60° resonator. The green curve, corresponding to the HFSS simulation, exhibits a resonance frequency of 2.8057 GHz with an S_{21} magnitude of -12.9736 dB. In contrast, the red curve, representing the experimental measurements obtained using the VNA, shows a resonance frequency of 2.8148 GHz with an S_{21} value of -13.2321 dB. Here, with a 60° angle, the Cesàro fractal coincides with the classical Koch curve, the folds provide longer and more interconnected current paths, improving the S_{21} value and making it more negative.

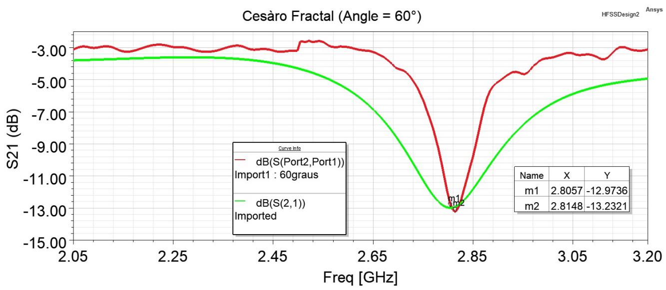

Fig. 17. Comparison of measured and simulated values for the 60-degree resonator.

Fig. 18 shows the measured and simulated resonance frequencies from the second-order fractal resonator with a 60° angle. In the figure, it can be observed that the resonance frequency simulated in HFSS, represented by the green curve, corresponds to an S_{21} value of -11.1049 dB at 3.4090 GHz, whereas the experimentally measured values, represented by the red curve, show a resonance frequency of 3.4400 GHz with a magnitude of -11.3555 dB.

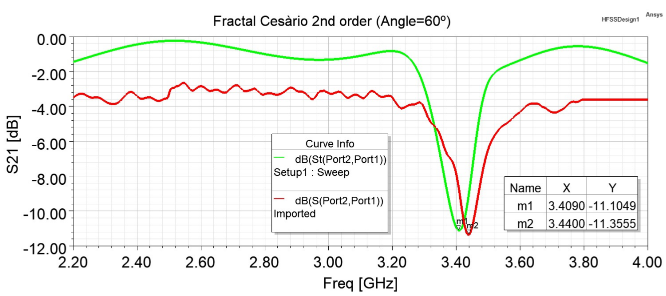

Fig. 18. Comparison of measured and simulated values for the second-order 60-degree resonator.

The small discrepancies observed in the comparisons of Figs. 15–18 are attributed to the use of SMA connectors and their associated solder joints in the fabricated prototypes. These elements introduce parasitic inductance and capacitance, which alter the resonant frequency, whereas ideal ports were assumed in the simulations.

Table II shows the values for each of the parameters, as well as the resonance and notch frequencies of each prototype, in addition to its base reduction.

TABLE II
PARAMETERS AND RESULTS OF THE FABRICATED RESONATORS

Variable	Order 1 (0°)	Order 1 (45°)	Order 1 (60°)	Order 2 (60°)	Unit
Dist	0.2	0.2	0.2	0.2	mm
Order	1	1	1	2	-
Wf	0.4	0.4	0.5	0.4	mm
Angle	0	45	60	60	degrees
Perimeter	70	70	70	70	mm
Segment	4.375	4.54	4.66	1.22	mm
Wsub	46	46	46	46	mm
H	1.6	1.6	1.6	1.6	mm
Lsub	70	70	70	70	mm
Wfeed	0.8	1	1	0.8	mm
t	0.017	0.017	0.017	0.017	mm
Frequency	2.6400	2.6595	2.8148	3.4400	GHz
Notch	-12.4574	-9.4731	-13.2321	-11.3555	dB
Base	17.5	15.5	14	11.05	mm
Base Reduction	-	11.43%	20%	36.86%	%

Table III was created for comparison with other works reported in the literature, showing the fractal type, the resonant frequency, the printed circuit board (PCB), the ϵ_r, the physical dimensions (in mm), and the electrical dimensions (in λ_g). The electrical dimensions were also included because they provide a fairer comparison between structures operating at different frequencies. Physical dimensions alone may not accurately reflect the level of miniaturization, whereas electrical dimensions relate the structure size to the guided wavelength, allowing a more meaningful comparison.

TABLE III
STATE OF THE ART FRACTAL RESONATORS REVIEWED IN THIS WORK

Fractal	Order	Frequency (GHz)	PCB	ϵ_r	Dimensions (mm)	Dimensions (λ_g)
Equilateral triangle [6]	0	2.7300	F4B-2	2.65	11.00 x 9.526	0.1629 x 0.1411
Koch snowflake [6]	1	2.1200	F4B-2	2.65	11.00 x 12.70	0.1265 x 0.1460
Koch snowflake [6]	2	1.8000	F4B-2	2.65	11.00 x 12.70	0.1074 x 0.1240
Minkowski [7]	2	2.9360	FR4	4.3	12.50 x 12.50	0.2536 x 0.2536
Square Loop [8]	0	0.9200	FR4*	4.4	20.90 x 20.90	0.1344 x 0.1344
Minkowski [8]	1	0.6350	FR4*	4.4	20.90 x 20.90	0.0927 x 0.0927
Minkowski [8]	2	0.4850	FR4*	4.4	20.90 x 20.90	0.0708 x 0.0708
Square Loop (this work)	0	2.6400	FR4	3.9	17.50 x 17.50	0.3041 x 0.3041
Cesàro 45° (this work)	1	2.6595	FR4	3.9	15.50 x 15.50	0.2713 x 0.2713
Cesàro 60° (this work)	1	2.8148	FR4	3.9	14.00 x 14.00	0.2594 x 0.2594
Cesàro 60° (this work)	2	3.4400	FR4	3.9	11.05 x11.05	0.2502 x 0.2502

In [8], the authors did not report the actual value of ϵ_r therefore, the standard value of $\epsilon_r = 4.4$ was adopted for this case. Since FR4 substrates may exhibit dielectric constant variations of up to 20% due to temperature effects and manufacturing tolerances [14], the adopted value should be considered an approximation. Table III shows that the Cesàro fractal exhibits a miniaturization potential comparable to that of previously published works, but offers the advantage of enabling resonant frequency tuning through variations in both perimeter and angle, as demonstrated herein.

V. CONCLUSIONS

This work presented an automated methodology for the design and miniaturization of RF resonators based on the Cesàro fractal curve for chipless RFID applications. Unlike conventional fractal geometries with fixed parameters, the tunable indentation angle of the Cesàro fractal was exploited as an additional degree of freedom, enabling independent control over both the resonant frequency and the physical footprint of the resonator. The parametric analysis demonstrated that the resonant frequency is primarily governed by the perimeter of the structure, while angular variation serves as an effective fine-tuning mechanism. Experimental results confirmed that increasing the indentation angle from 0° to 60° reduced the base dimension from 17.5 mm to 14.0 mm, corresponding to a 20% size reduction relative to the conventional square-loop resonator. The close agreement between simulated and measured S_{21} responses across all fabricated prototypes validates both the accuracy of the electromagnetic model and the reliability of the Python-based automation framework. The proposed approach significantly reduces design complexity by eliminating the need for manual geometry construction in HFSS, enabling rapid parametric exploration of fractal configurations. These results establish the Cesàro fractal as a promising and flexible alternative to existing fractal geometries for compact chipless RFID resonator design. Future work may extend this methodology to multibit tag configurations and explore higher-order fractal iterations.

REFERENCES

[1] K. Finkenzeller, RFID Handbook: Fundamentals and Applications in Contactless Smart Cards, Radio Frequency Identification and Near-Field Communication, 3rd ed. Wiley, 2010. doi :10.1002/9780470665121

[2] S. Preradovic and N. C. Karmakar, "Chipless RFID: Bar code of the future," IEEE Microwave Magazine, vol. 11, no. 7, pp. 87-97, Dec. 2010. doi: 10.1109/MMM.2010.938571

[3] R. K. Mishra, P. Sethy and S. K. Behera, "Chipless RF Identification Sensors for Product Tracking and Identification Applications: A Review," in IEEE Microwave Magazine, vol. 26, no. 8, pp. 64-86, 2025, doi: 10.1109/MMM.2025.3563058.

[4] S. Preradovic, I. Balbin, N. C. Karmakar and G. F. Swiegers, "Multiresonator-Based Chipless RFID System for Low-Cost Item Tracking," in IEEE Transactions on Microwave Theory and Techniques, vol. 57, no. 5, pp. 1411-1419, May 2009, doi: 10.1109/TMTT.2009.2017323.

[5] D. H. Werner and S. Ganguly, "An overview of fractal antenna engineering research," IEEE Antennas and Propagation Magazine, vol. 45, no. 1, pp. 38-57, Feb. 2003. doi: 10.1109/MAP.2003.1189650

[6] H. Zeng, G. Wang, J. Liang, and X. Gao, "Complementary split ring resonators using equilateral triangular Koch fractal curves," in 2009 3rd IEEE International Symposium on Microwave, Antenna, Propagation and EMC Technologies for Wireless Communications, 2009, pp. 911-913, doi: 10.1109/MAPE.2009.5355780.

[7] N. Nantapanich et al., "Miniaturization of Dimensions Based on Square Loop Resonator with NP Fractal Model for Sensor Applications," in 2025 13th International Electrical Engineering Congress (iEECON), 2025, pp. 1-4, doi: 10.1109/iEECON64081.2025.10987705.

[8] A. Govindankutty et al., "On Using Square-Shaped Fractal Patterns to Reduce the Operating Frequency of Open Complementary Split Ring Resonators on a Single Conducting Layer," in 2024 IEEE International Symposium on Antennas and Propagation and INC/USNC-URSI Radio Science Meeting (AP-S/INC-USNC-URSI), 2024, pp. 957-958, doi: 10.1109/AP-S/INC-USNC-URSI52054.2024.10686365.

[9] H.-L. Peng et al., "Compact Tunable Bandpass Filter With a Fixed Out-of-Band Rejection Based on Hilbert Recent," IEEE Transactions on Components, Packaging and Manufacturing Technology, vol. 3, no. 3, pp. 391-400, 2013, doi: 10.1109/TCPMT.2012.2222643.

[10] N. Janković, R. Geschke, and V. Crnojević-Bengin, "Compact Tri-Band Bandpass and Bandstop Filters Based on Hilbert-Fork Resonators," IEEE Microwave and Wireless Components Letters, vol. 23, no. 6, pp. 282-284, June 2013, doi: 10.1109/LMWC.2013.2258005.

[11] R. K. Abdulsattar, T. A. Elwi, and Z. A. A. Hassain, "Microwave Resonator based a Fractal Moore Structure for Modern Wireless Reconfigurable Systems" in 2021 3rd International Conference on Research and Academic Community Services (ICRACOS), 2021, pp. 98-102, doi: 10.1109/ICRACOS53680.2021.9701943.

[12] A. S. A. Jalal and A. Ismail, "A compact fractal-based asymmetrical dipole antenna for RFID tag applications," in 2018 Third Scientific Conference of Electrical Engineering (SCEE), 2018, pp. 101-104. doi: 10.1109/SCEE.2018.8684136

[13] L. A. C. Fonseca, H. E. Hernandez-Figueroa, G. T. Santos-Souza and L. L. Bravo-Roger, "Dielectric Properties Characterization: A Simple Inverse Problem Approach," 2017 IEEE MTT-S International Conference on Numerical Electromagnetic and Multiphysics Modeling and Optimization for RF, Microwave, and Terahertz Applications (NEMO), pp. 22-24, 2017, doi: 10.1109/NEMO.2017.7964174.

[14] P. Sagar and K. Akber, "Studies on temperature dependent dielectric properties of some insulators down to liquid helium temperatures," *Cryogenics*, Jun. 2024, Art. no. 103865, doi: 10.1016/j.cryogenics.2024.103865.

Gabriel São Martinho da Silva graduated in Telecommunications Engineering from the State University of Campinas (UNICAMP) in 2023 and is currently pursuing a master's degree in Technology. He has an interest in the areas of radio frequency and machine learning.

Rodrigo Luiz Ximenes received his Bachelor's degree in Telecommunications Technology from the University of Campinas (UNICAMP), Brazil. He obtained his Master's degree in Technology in 2015 and his Ph.D. degree in Technology in 2025, both from UNICAMP. He is currently responsible for the Embedded Systems Laboratory at the UNICAMP campus in Limeira, São Paulo, Brazil.

Lisandro Manuel De la Torre Rodríguez received his bachelor's degree in Telecommunications and Electronics Engineering in 2003 from the University of Oriente, Santiago de Cuba. In 2007, he obtained a Master's degree in New Technologies for Education from the same institution. In 2017, he earned his Ph.D. in Electrical Engineering from the University of Campinas. His main research interests include RFID and antenna design, electromagnetics, metamaterials, and the application of Machine Learning and Artificial Intelligence for predictive analysis in healthcare and engineering.

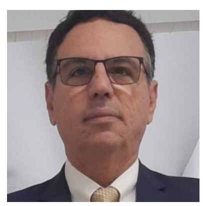

Leonardo Lorenzo Bravo Roger is currently the Director of the School of Technology at the University of Campinas (UNICAMP), where he was recently approved for the position of Full Professor. He received his Livre Docente title in November 2018 and his Ph.D. in Electrical Engineering from UNICAMP in 2003. His primary research interests include Radio Frequency Sensing, Radio Frequency Machine Learning Systems (RFMLS), Antennas, RF and Microwave Technologies, Radio Frequency Identification (RFID), Terahertz Identification (THID), Metamaterials, Nanotechnology, Wireless Sensor Networks, Mobile and Optical Communications, Finite Element Simulations, Ultrashort Pulse and Plasmonic Wave Propagation, Radio Wave Propagation, and Applied Electromagnetism.